(Small et al., 2006; Thompson et al., 2009). Thus, better tau radioligands with higher affinity for tau fibrils and/or less nonspecific binding to tissues are urgently needed to complement high-contrast senile plaque imaging agents, including widely studied [^{11}C]Pittsburgh Compound-B ([^{11}C]PIB) (Klunk et al., 2004) and United States Food and Drug Administration-approved [^{18}F]florbetapir (Yang et al., 2012). In addition, [^{18}F]FDDNP and several other candidate tau probes do not bind to tau inclusions in non-AD tauopathy brains without plaque deposition (Okamura et al., 2005) and therefore can be clinically characterized only in AD patients with comingled Aβ and tau amyloids. Hence, compounds that detect diverse tau aggregates, including tau inclusions in non-AD neurodegenerative diseases and tau Tg models, could be used to interrogate in vivo interactions between exogenous ligands and tau pathologies.

Here, we found that the lipophilicity of β sheet ligands is associated with their selectivity for tau versus Aβ fibrils and that the core dimensions of these chemicals are major determinants of their reactivity with a broad spectrum of tau aggregates in diverse tauopathies and mouse models of tau pathology. Building on these observations, we developed a series of fluorescent compounds capable of detecting diverse tau lesions using optical and PET imaging in living Tg mouse models of tauopathies. Finally, we identified a radiotracer that produced the highest contrast for tau inclusions in animal PET and used it in exploratory in vivo imaging studies of AD patients, providing clear demonstration of signal intensification in tau-rich regions, in sharp distinction to [^{11}C]PIB-PET data reflecting plaque deposition.

RESULTS

Identification of PBBs as Ligands for Diverse Tau Inclusions in Human Tauopathies

We screened an array of fluorescent chemicals capable of binding to β sheet conformations (see the Compounds subsection in the Experimental Procedures). Fluorescence labeling with these compounds were examined in sections of AD brains bearing Aβ and tau amyloids (Figures 1A and 2A) and non-AD tauopathy brains characterized by tau inclusions and few or no Aβ plaques (Figure 2). Amyloid PET tracers currently used for human PET studies, PIB (Klunk et al., 2004), and BF-227 (Kudo et al., 2007), tightly bound to senile plaques, while they only weakly reacted with AD NFTs (Figures 1A; Figure S1 available online). PET probes reported to selectively label tau aggregates, BF-158 (Okamura et al., 2005) and THK523 (Fodero-Tavoletti et al., 2011), detected AD NFTs (Figures 2A and S1) but microscopically detectable fluorescence signals produced by FDDNP, which are presumed to bind to both Aβ and tau fibrils (Small et al., 2006), were consistent with dense cores of classic plaques and distinct from tau lesions (Figures 2A and S1). None of the above-mentioned PET ligands were reactive with tau inclusions in non-AD tauopathies, such as Pick bodies in Pick's disease (Figures 2A and S1) and neuronal and glial fibrillary lesions in PSP and CBD (data not shown). By contrast, these pathologies were intensely labeled with a widely used amyloid dye, thioflavin-S, and a derivative of another classic amyloid dye Congo red, (E,E)-1-fluoro-2,5-bis(3-hydroxycarbonyl-4-hydroxy)styrylbenzene (FSB) (Higuchi et al., 2005; Maeda et al., 2007) (Figures 1, 2A, and S1), although these chemicals may not undergo efficient transfer through the blood-brain barrier (BBB) (Zhuang et al., 2001). Because compounds possessing a π-electron-conjugated backbone longer than 13Å exhibited affinities for pathological inclusions in a broad range of tauopathies, we examined binding of additional chemicals with a variety of structural dimensions to tau aggregates and found that affinity for non-AD tau inclusions could be attributed to a core structure with a specific extent ranging from 13 to 19 Å (Figure S1). Based on this view and the known fact that chemicals with a flat and slender backbone could pass through and attach to channel-like accesses in β-pleated sheets (Krebs et al., 2005), we developed a class of compounds, phenyl/pyridinyl-butadienyl-benzothiazoles/benzothiazoliums (PBBs), by stretching the core structure of a prototypical fluorescent amyloid dye, thioflavin-T, with two C = C double bond inserts between aniline (or aminopyridine) and benzothiazole (or benzothiazolium) groups (Figure 1B).

All PBB compounds intensely labeled NFTs, neuropil threads, and plaque neurites in AD brains (Figure 1C). Interestingly, the affinity of these PBBs for Aβ plaques lacking dense cores was positively correlated with their lipophilicity (Figure 1C), and thereby three potential probes with relatively low logP (log of the octanol/water partition coefficient) values, including PBB3, 2-[4-(4-methylaminophenyl)-1,3-butadienyl]-benzothiazol-5,6-diol (PBB4) and PBB5 (structurally identical to Styryl 7, CAS registry number 114720-33-1), appeared suitable for visualizing tau pathologies in living organisms with reasonable selectivity. High-affinity of PBBs for tau lesions was further demonstrated by fluorometric analyses using Aβ and tau filaments assembled in a test tube (Table S1; experimental procedures are given in the Supplemental Experimental Procedures), but the most and least lipophilic PBB members displayed similar selectivity for in vitro tau versus Aβ pathologies, implying a methodological limitation in screening chemicals for tau-selective ligands based on binding to synthetic peptides and recombinant proteins. PBBs and FSB were also shown to label tau inclusions in non-AD tauopathies, such as Pick's disease (Figures 2A and S1), PSP, and CBD (Figure 2B), all of which were immunodetected by an antibody specific for phosphorylated tau proteins (AT8).

In Vitro and Ex Vivo Fluorescence Imaging of Tau Lesions in Tau Tg Mice by PBBs

To obtain in vivo evidence of direct interaction between PBBs and tau lesions, we employed Tg mice expressing a single human four-repeat tau isoform with the P301S FTDP-17 mutation (PS19 line, see Figure S2 for neuropathological features of this Tg strain) (Yoshiyama et al., 2007). Similar to the findings in non-AD tauopathy brains, NFT-like inclusions in the brain stem and spinal cord of PS19 mice were clearly recognized by PBBs (Figures 3A and S1). We then performed ex vivo fluorescence labeling of tau lesions in PS19 mice with intravenously administered PBBs. Brains and spinal cords were removed 60 min after tracer injection, and fluorescence microscopy revealed an intense accumulation of these compounds in fibrillary tau inclusions abundantly seen throughout the sections by

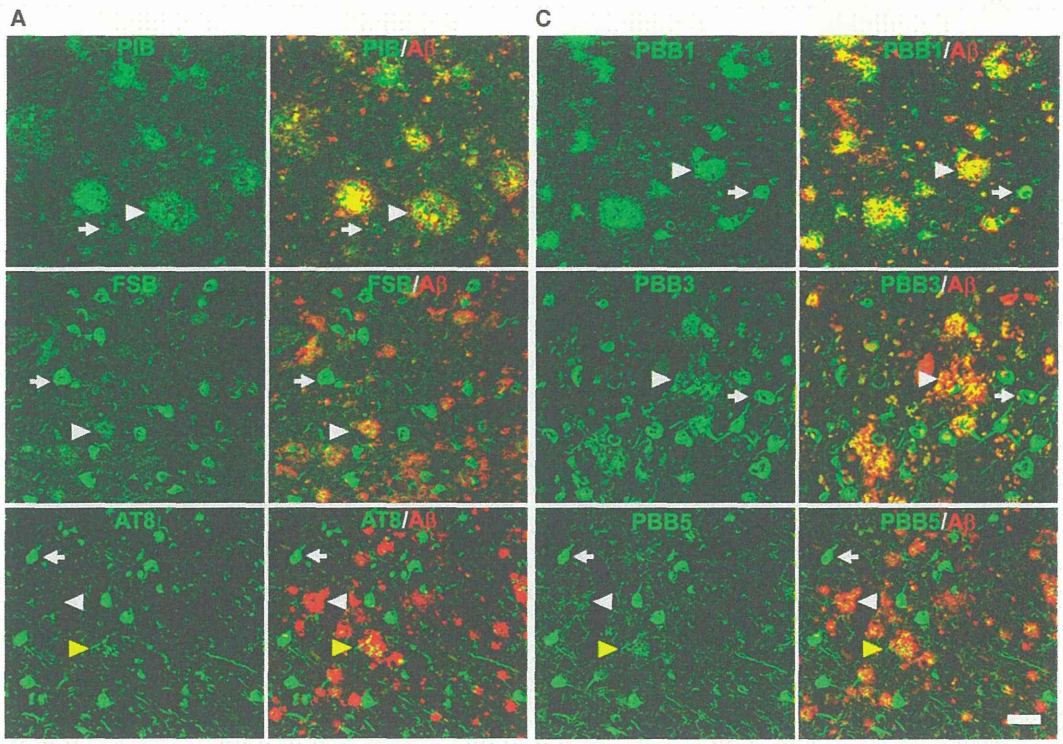

B

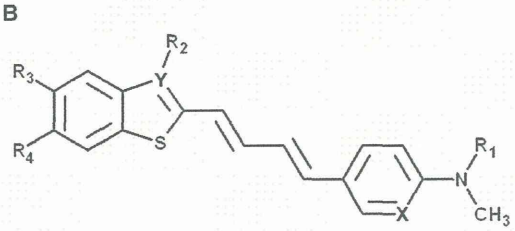

Compound	R_1	R_2	R_3	R_4	X	Y	ClogP
PBB1	CH_3	-	H	H	C(H)	N	5.44
PBB2	H	-	H	OH	C(H)	N	3.57
PBB3	H	-	H	OH	N	N	3.30
PBB4	H	-	OH	OH	C(H)	N	2.97
PBB5	CH_3	CH_3CH_2	H	H	C(H)	N^+	2.32

Figure 1. Design and Characterization of PBB Compounds as Potential Imaging Agents for Tauopathies

(A) Confocal fluorescence images of frontal cortex sections from an AD patient. Following fluorescence labeling (pseudocolors are converted to green) with PIB (top row) and FSB (middle row), the samples were immunostained with an antibody against AβN3(pE) (red in the right column). PIB intensely labeled Aβ plaques (white arrowheads) but did not clearly label NFTs (arrows). By contrast, NFTs and neuropil threads were intensely labeled by FSB, whereas the staining of diffuse plaques was negligible. A section was also doubly immunolabeled (bottom row) with AT8 (green) and anti-AβN3(pE) antibodies (red in the right panel), to demonstrate the abundance of tau and Aβ amyloids in this area. Yellow arrowheads indicate tau-positive dystrophic neurites associated with senile plaques.

(B) Structures of PBBs. Neutral benzothiazoles (PBB1-4) are newly synthesized chemicals, and a charged benzothiazolium, PBB5, is identical to a commercially available near-infrared laser dye.

(C) Confocal fluorescence images of PBBs (pseudocolors are converted to green) and AβN3(pE) (red in the right column) staining in sections adjacent to those displayed in (A). The intensity of plaque staining (arrowheads) relative to that of NFTs (arrows) was positively associated with the lipophilicity of PBBs. As compared with PBB1 (top row) staining, labeling of diffuse plaques with PBB3 (middle row) was substantially attenuated. PBB5 was nearly unreactive with diffuse plaques (bottom row), and subsequent double immunofluorescence staining of the same section (bottom row in C) illustrated good agreement of PBB5 labeling with the distribution of AT8-positive NFTs.

Scale bar, 50 μm (A and C). See also Figure S1 and Table S1.

staining with thioflavin-S, FSB, and AT8 (Figure 3B). On the other hand, no overt in vitro (Figure 3A) or ex vivo (data not shown) fluorescence of these ligands was noted in the corresponding regions of non-Tg wild-type (WT) mice. Consistent with these observations, two-photon laser scanning fluorescence microscopy of ex vivo samples demonstrated somatic and neuritic staining of a subset of tangle-bearing neurons with intravenously injected 2-[4-(4-methylaminophenyl)-1,3-butadienyl]-benzothiazol-6-ol (PBB2) and PBB4 in unsliced spinal cord blocks from PS19 mice (Figure 3B).

In Vivo Macroscopic and Mesoscopic Optical Detection of Fibrillar Tau Pathologies in a Mouse Model Using PBB5

We next characterized PBBs with the use of in vivo fluorescence imaging modalities, which permitted a quick assessment of

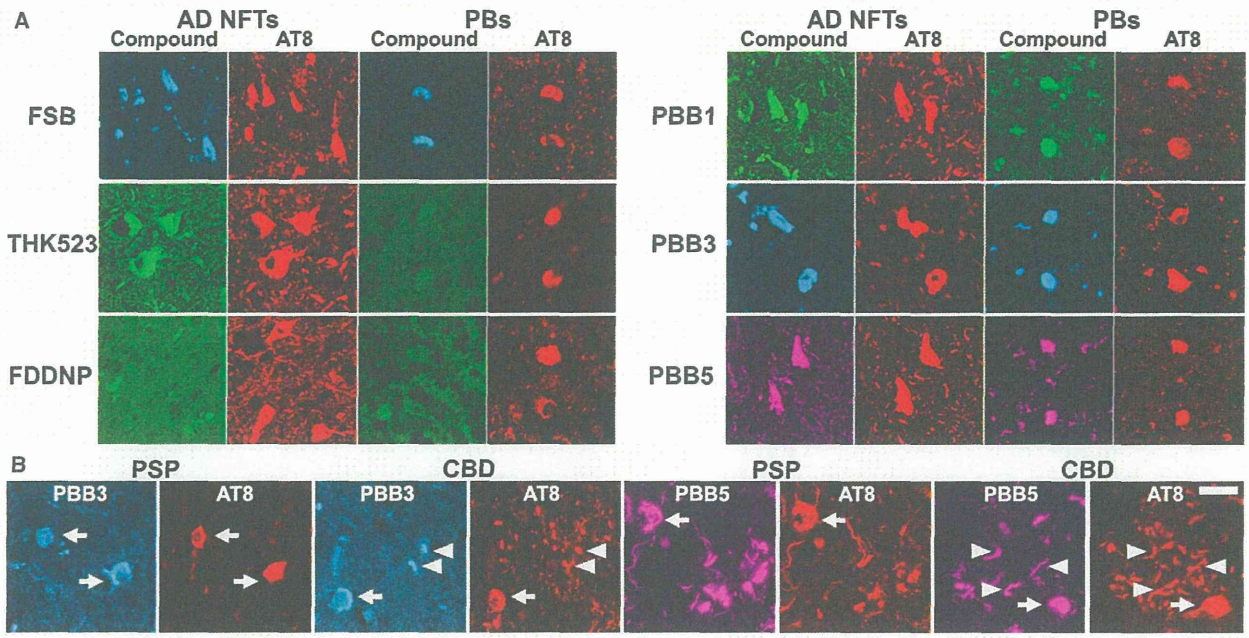

Figure 2. Binding of Tau Ligands to Tau Lesions in AD and Non-AD Tauopathy Brains

(A) Double fluorescence staining of AD NFTs and Pick bodies (PBs) in Pick's disease with PBBs, other tau ligands, and anti-phospho-tau antibody (AT8). FSB and PBBs sensitively captured AD NFTs and PBs. AD NFTs were labeled with THK523. Meanwhile, PBs were not visualized by these compounds. NFTs and PBs were barely recognizable by using FDDNP.

(B) Double fluorescence staining of neuronal tau inclusions (arrows) in PSP and CBD and putative astrocytic plaques (arrowheads) in CBD. A substantial portion of tau fibrils in neurons were captured by PBB3 and PBB5, but a much smaller subset of phosphorylated tau aggregates in astrocytic plaques were labeled with these compounds.

Scale bar, 20 μm (A and B). See also Figures S2 and S3.

candidate chemicals without the need for radiolabeling. Because PBB5 is fluorescent, with peak excitation and emission wavelengths in a near-infrared range (Table S1), this compound is applicable to in vivo optical imaging of tau deposits in laboratory animals. To examine this possibility, fluorescence images were obtained from living mice over a time course following intravenous PBB5 injections using a small animal-dedicated system permitting the intravital observation of fluorescence signals at magnifications varying between macroscopic and microscopic levels. Tail vein administration of PBB5 in PS19 mice revealed strong fluorescence relative to non-Tg WT mice in the central nervous system (CNS) above the slit between the base of the skull and first vertebra, through the skin and connective tissues overlaying the cisterna magna (Figures S3A–S3D), suggesting a concentration of this tracer in the PS19 spinal cord. In line with this in vivo observation, the hindbrain and spinal cord of PS19 mice, which were dissected out at 2 hr after the injection of PBB5, exhibited increased retention of this compound compared to non-Tg WT mice (Figures S3E–S3G).

In vivo optical imaging of tau Tg mice was subsequently performed using a device equipped with a pulsed diode laser and a photomultiplier tube to detect deep signals through the skull. Elevated levels of fluorescence intensity were found in homogenized brain stem samples collected from PS19 mice at 20 hr after the intravenous tracer administration (Figure S4A), indicating a long-lasting in vivo binding of PBB5 to tau fibrils. To support the ex vivo evidence, fluorescence intensity was noninvasively analyzed in living PS19 and non-Tg WT mice treated with PBB5. The mice, with their heads shaved in advance, were prescanned, and autofluorescence signals were detected at a relatively high level in an area corresponding to the frontal forebrain. Using these baseline signals as landmarks, regions of interest (ROIs) were defined in the frontal cortex, brain stem, and spinal cord (Figure 4A). The near-infrared fluorescence was notably increased immediately after the intravenous injection of PBB5 (Figure S4C), and the fluorescence in the brain stem and spinal cord ROIs of PS19 mice much exceeded that in WT mice at 30 min (Figure 4B). Fluorescence intensity in the frontal cortex ROI, normalized on the basis of integration time and laser power, was lower in PS19 mice than in WT mice over 120 min after tracer injection (Figure S4B), which may reflect impaired CNS delivery of the tracer in Tg mice due to degenerative changes (see Figures S4C–S4L for details), and thereafter this became almost equivalent between the two genotypes (Figure S4B). Meanwhile, persistent retention of the signals in the brain stem and spinal cord ROIs of PS19 mice was observed beyond 240 min (Figures 4B and S4B). A more quantitative index comparable among different mice was determined by calculating the target-to-frontal-cortex ratio of fluorescence intensity and was shown to increase over time particularly in PS19 mice (Figures 4C and 4D). This ratio was significantly greater in PS19 mice than in WT mice at 240 min (Figure 4E), beyond which the difference

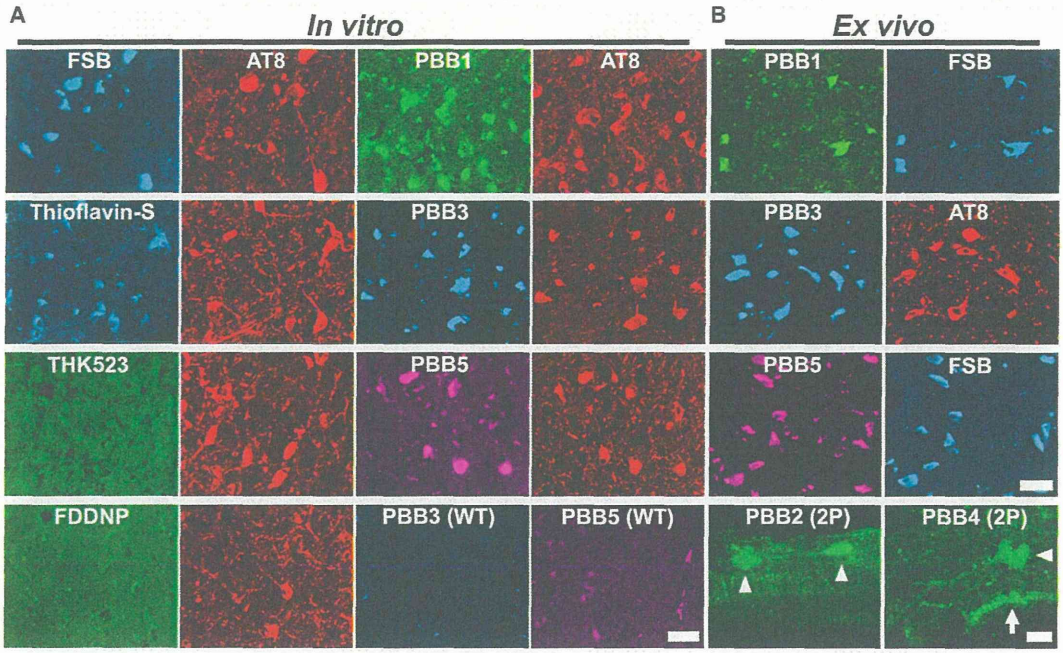

Figure 3. In Vitro and Ex Vivo Labeling of NFTs in PS19 Mice with PBB Compounds

(A) Double fluorescence staining of intraneuronal tau aggregates in postmortem brain stem slices of a 12-month-old PS19 mouse with PBB, other amyloid ligands, and anti-phospho-tau antibody (AT8).

(B) Binding of intravenously administered PBBs (0.1 mg/kg PBB5 and 1 mg/kg PBB1 and PBB3) to NFTs in PS19 mice at 10–12 months of age. The tissues were sampled at 60 min after tracer administration. The brain stem (top row) and spinal cord (second and third rows from the top) sections abundantly contained neurons showing strong fluorescence (left), and subsequent staining with FSB or AT8 (right) indicated that these cells were laden with tau amyloid fibrils (right). Putative intraneuronal tau inclusions in unsectioned spinal cords (arrowheads in the bottom row) removed from PS19 mice at 60 min after intravenous injection of PBB2 and PBB4 were also clearly visible by using a two-photon (2P) fluorescence microscopic system. Arrow in the bottom row indicates a cluster of autofluorescence signals from blood cells.

Scale bars, 25 μm (A), 30 μm (top to third rows in B), and 20 μm (bottom row in B).

between the two lines of mice became nearly constant (Figures 4C and 4D). The intensity ratio of the spinal cord ROI to the frontal cortex in PS19 mice at 240 min was also significantly correlated with the abundance of NFTs stained with FSB (Figure 4F), but such correlations were not statistically significant in the brain stem (Figure 4F), implying limitations of the intensitometry in some brain regions below the cerebellum and fourth ventricle.

Intravital Imaging of Individual Tau Inclusions by PBB3 and Two-Photon Laser Scanning Fluorescence Microscopy

Two-photon excitation microscopy, which enables optical sectioning, potentially up to 1 mm deep, in living tissues, could be utilized to visually demonstrate transfer of a fluorescent probe from the plasma compartment into the cytoplasm of CNS neurons and binding of the probe to intraneuronal tau inclusions. We therefore captured fluorescence signals from intravenously administered PBB3 by in vivo two-photon laser scanning microscopic imaging of the spinal cord of laminectomized PS19 mice. Within 3 s of PBB3 injection, green fluorescence signals emerged in blood vessels prelabeled with red with intraperitoneal treatment using sulforhodamine 101 and subsequently diffused from the vasculatures to the spinal cord parenchyma over the next few minutes (Figures 5A–5F). These diffuse signals declined thereafter due to the clearance of PBB3 from the tissue, whereas intense labeling of putative tau inclusions with green fluorescence appeared in a subpopulation of large cells morphologically identified as neurons at 3–5 min after PBB3 injection (Figures 5G and 5H). These intracellular PBB3 fluorescent signals were not found in the spinal cord of WT mice (Figure 5I). As the BBB of the brain and spinal cord are presumed to be identical, the two-photon microscopic data obtained here provide compelling evidence that PBB3 rapidly transits the BBB and neuronal plasma membranes, where it binds to intraneuronal tau inclusions. Accumulation of injected PBB3 in AT8-positive, NFT-like lesions of Tg mice was postmortemly confirmed by ex vivo microscopy (Figures 5J and 5K).

Autoradiographic and PET Imaging of Tau Lesions in PS19 Mice by Radiolabeled PBBs

We investigated the kinetic properties of PBBs by high-performance liquid chromatography (HPLC) analyses of plasma and brain samples collected from non-Tg WT mice treated with these ligands. Following intravenous administration, PBB5 was rapidly converted into a major metabolite, which at 5 min was found at high levels in both plasma and brain extracts. Subsequent liquid

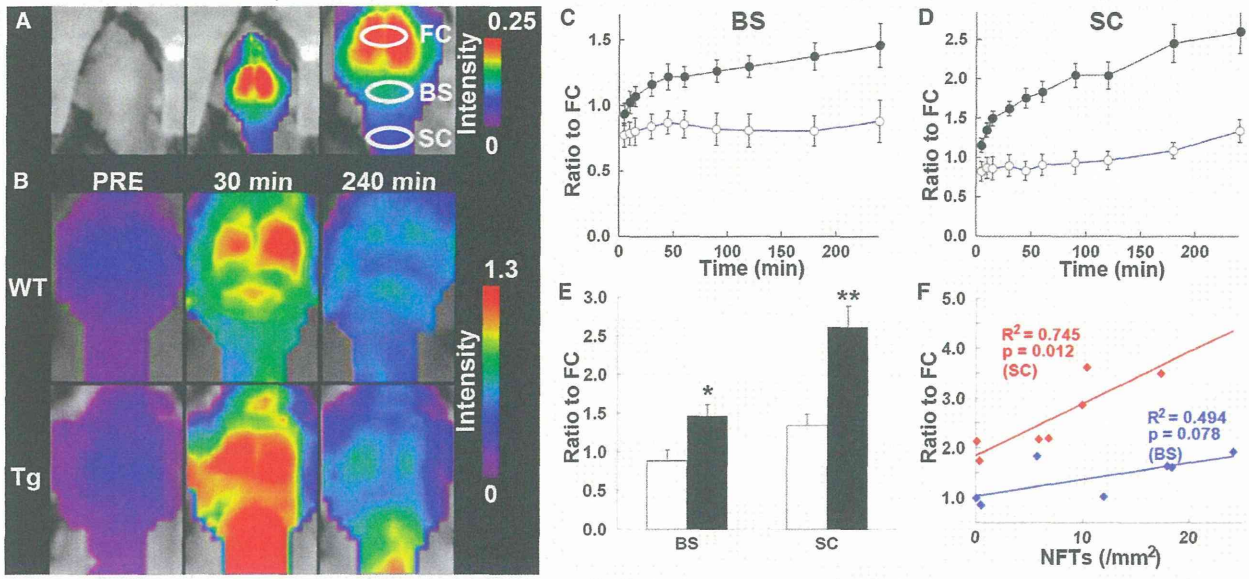

Figure 4. Noninvasive Near-Infrared Imaging of Tau Pathology in Living Tau Tg Mice Using Pulsed Laser Optics and PBB5

(A) Baseline autofluorescence signals (middle) are overlaid on the visible background image of a shaven non-Tg WT mouse head (left). Ellipsoidal ROIs are defined above the frontal cortex (FC), brain stem (BS), and cervical spinal cord (SC) guided by a relatively intense emission from the FC region (right).

(B) Fluorescence intensity maps in 12-month-old WT (top) and PS19 (Tg; bottom) mice before and at 30 and 240 min after the intravenous administration of PBB5 (0.1 mg/kg). The intensity maps (A and B) are normalized by the FC ROI value at 30 min after tracer injection. Long-lasting retention of the tracer was noted in the BS and SC ROIs of the Tg mouse.

(C and D) Target-to-FC ratios of fluorescence intensity in the BS (C) and SC (D) ROIs over the image acquisition time in the WT (open circles; n = 7) and PS19 (closed circles; n = 7) mice. There were significant main effects of time, region, and genotype in two-way, repeated-measures ANOVA (time, $F_{(11, 132)} = 17.6$, $p < 0.001$; region, $F_{(1, 12)} = 29.9$, $p < 0.001$; genotype, $F_{(1, 12)} = 23.6$, $p < 0.001$).

(E) Target-to-FC ratios in the BS and SC ROIs of the WT (open columns) and tau Tg (closed columns) mice at 240 min after tracer injection. *$p < 0.05$; **$p < 0.01$; two-way repeated-measures ANOVA with Bonferroni's post hoc analysis.

(F) Scatterplots of target-to-FC ratios at 240 min versus the number of FSB-positive NFTs per unit area of postmortem 20 μm tissue slices in BS (blue symbols) and SC (red symbols) ROIs of tau Tg mice. Solid lines represent regressions; p values were determined by t test. Vertical bars in the graphs represent SEs.

See also Figures S3 and S4.

chromatography-mass spectrometry (LC-MS) assays suggested that the major metabolite was likely a reduced, electrically neutralized derivative of PBB5 (Figures S5A and S5B). Besides transventricular uptake of unmetabolized PBB5 as implied above, this uncharged form incapable of emitting near-infrared light could readily penetrate the BBB, as well as cell membranes, and thereafter could be reoxidized into its original form, thereby enabling it to bind to tau fibrils, particularly at sites exposed to oxidative stress in pathological conditions. In addition, PBB4 was promptly converted to metabolites capable of entering the brain. Finally, studies of PBB2 and PBB3 showed that they exhibited reasonable biostability and sufficient entry into and clearance from the brain. Indeed, HPLC assays demonstrated that fractions of unmetabolized PBB2 and PBB3 in mouse plasma were 23.5% and 16.3%, respectively, at 3 min after intravenous administration and were 4.6% and 2.8%, respectively, at 30 min. There were also no metabolites of PBB2 and PBB3 detectable in the mouse brain at 3 and 30 min.

We then radiolabeled PBB2 and PBB3 with ^{11}C to conduct autoradiographic and PET assays using PS19 mice. In vitro autoradiography using frozen tissue sections showed binding of these radioligands to the brain stem of PS19 mice and neocortex of AD patients (Figure 6A). As expected from their lipophilicities, [^{11}C]PBB3 yielded high-contrast signals with less nonspecific labeling of myelin-rich white matter than did [^{11}C]PBB2, and the accumulation of [^{11}C]PBB3 in pathological regions was nearly completely abolished by the addition of nonradioactive compounds. Similarly, ex vivo autoradiographic studies demonstrated that intravenously administered [^{11}C]PBB3 selectively labeled the brain stem and spinal cord of PS19 mice harboring neuronal tau inclusions, whereas tau-associated [^{11}C]PBB2 radiosignals were less overt because of a considerable level of nonspecific background (Figure 6B; Figures S6C–S6F). Finally, in vivo visualization of tau lesions in PS19 mouse brains was enabled by a microPET system using these two tracers (Figures 6C, S6A, and S6B). Following intravenous injection, [^{11}C]PBB3 rapidly crossed the BBB and unbound and nonspecifically bound tracers were promptly washed out from the brain with a half-life of ~10 min (left panel in Figure 6E). The retention of [^{11}C]PBB3 signals in the brain stem of 12-month-old PS19 mice lasted over the imaging time (90 min), producing a pronounced difference from that in age-matched non-Tg WT mice (left panel in Figure 6E). By selecting the striatum as a reference region lacking tau deposits, the target-to-reference ratio was estimated for the brain stem, with the value in PS19 mice peaking at around 70 min, contrasting with its continuous decrease over

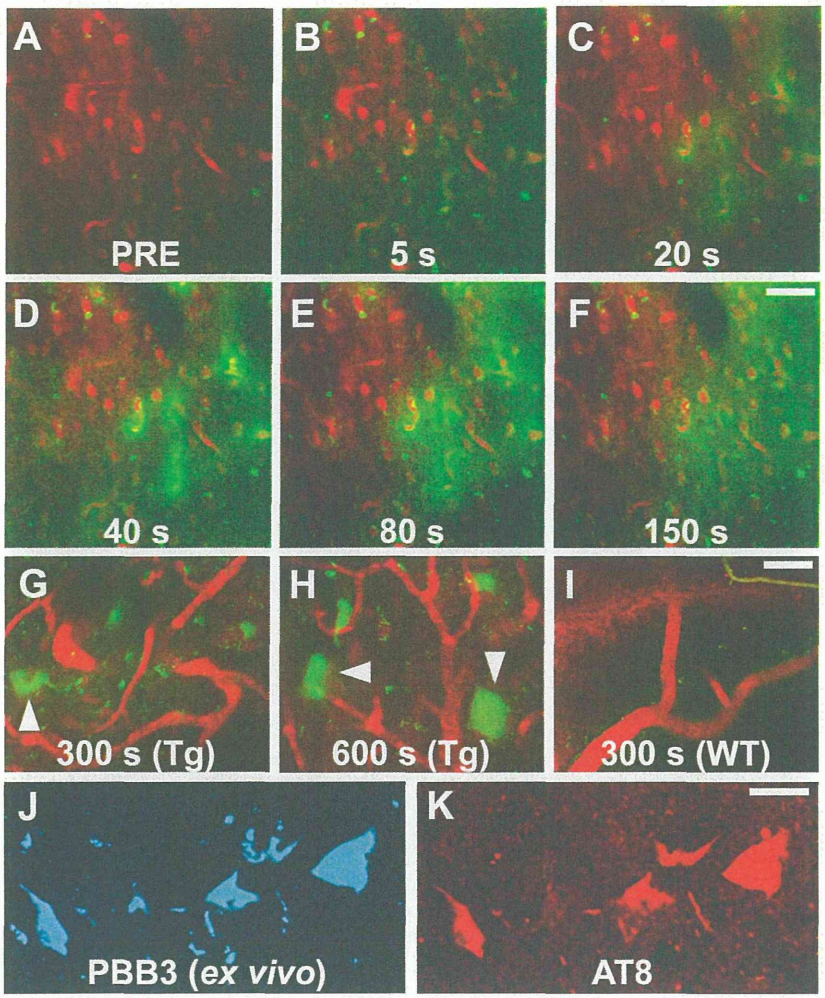

Figure 5. Real-Time Two-Photon Laser Scanning Images of PBB3 Diffusing from Vessels, Binding to Intraneuronal Tau Inclusions, and Clearing from Spinal Cord

(A–H) A maximum projection of fluorescence in a 3D volume of the spinal cord of a living PS19 mouse at 12 months of age before (A) and at various time points after (B–H) intravenous administration of PBB3 (1 mg/kg). Blood vessels were labeled with sulforhodamine 101 (red) intraperitoneally injected at 15 min before PBB3 administration. Green fluorescence indicates a rapid transfer of PBB3 from the plasma to tissue parenchyma (B–E) and subsequent washout from the tissue (F). Background PBB3 signals were further attenuated beyond 300 s, whereas somatodendritic labeling by this compound was observed in a subset of neurons (arrowheads in G and H).

(I) Fluorescence image of WT spinal cord at 300 s after PBB3 injection demonstrates no overt retention of the tracer in the tissue.

(J and K) Ex vivo microscopy for a brain stem section of the same Tg mouse. Tissues were obtained at 60 min after PBB3 injection. Signals of intravenously administered PBB3 (J) overlapped with AT8 immunoreactivity (K).

Scale bars, 50 μm (A–F), 25 μm (G–I), and 25 μm (J and K).

60 min in WT mice (right panel in Figure 6E). The mean ratio at 45–90 min was increased by 40% in 12-month-old PS19 mice as compared with age-matched WT mice ($p < 0.01$ by t test). The agreement between localizations of PET signals and tau inclusions in PS19 mice was proven by postmortem FSB staining of brain sections from scanned mice (Figure 6D). Significantly, the mean target-to-reference ratio in the brain stem quantified by PET correlated closely with the number of FSB-positive inclusions per brain section in the same region of the postmortem sample ($p < 0.001$ by t test; data not shown). [^{11}C]PBB2 exhibited slower clearance from the brain and higher nonspecific retention in myelin-rich regions than [^{11}C]PBB3 (Figure S6G), resulting in insufficient contrast of tau-bound tracers in the brain stem of PS19 mice and a small difference in the target-to-reference ratio of radioactivities between PS19 and WT mice (8% at 45–90 min; $p < 0.05$ by t test; Figure S6H) relative to those achieved with [^{11}C]PBB3.

As radiolabeling at the dimethylamino group in PBB5 with ^{11}C was unsuccessful, ^{11}C-methylation of a hydroxyl derivative of this compound was performed, leading to the production of [^{11}C]methoxy-PBB5 ([^{11}C]mPBB5; Figure S5C). PET images demonstrated complex pharmacokinetics of [^{11}C]mPBB5 (Figures S5D and S5E), and the difference in the specific radioligand binding between Tg and WT mice was small relative to the [^{11}C]PBB3-PET data (Figure S5F). After taking all of these findings into consideration, [^{11}C]PBB3 was selected as the most suitable ligand for in vivo PET imaging of tau pathology in tau Tg mice and human subjects.

Notably, the hippocampus of many PS19 mice was devoid of overt [^{11}C]PBB3 retention (Figure 6C), although a pronounced hippocampal atrophy was noted in these animals. This finding is in agreement with the well-known neuropathological features of PS19 mice in the hippocampus, because the accumulation of AT8-positive phosphorylated tau inclusions results in the degeneration of the affected hippocampal neurons prior to or immediately after NFT formation, followed by the clearance of their preNFTs or NFTs that are externalized into the interstitial CNS compartment (Figure S2). To explore the feasibility of our imaging agents in studies with other tauopathy model mice, we also performed fluorescence labeling with PBBs for brain sections generated from rTg4510 mice (Santacruz et al., 2005; the Supplemental Experimental Procedures). As reported elsewhere (Santacruz et al., 2005), these mice developed numerous thioflavin-S-positive neuronal tau inclusions in the neocortex and hippocampus, and reactivity of these lesions with PBBs was demonstrated by in vitro and ex vivo fluorescence imaging (Figure S7).

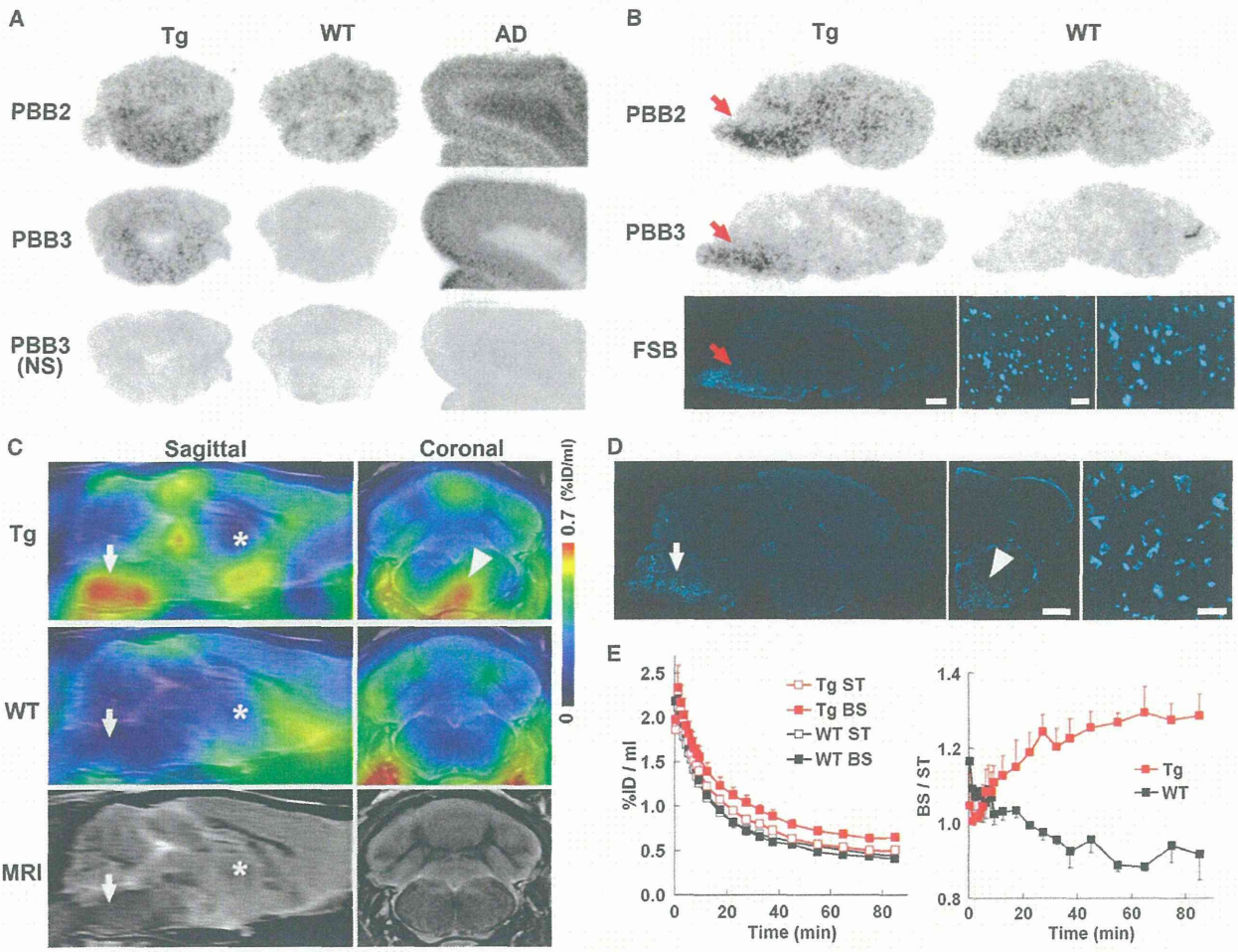

Figure 6. PET and Autoradiographic Detection of Tau Pathologies in PS19 Mice Using [^{11}C]PBB2 and [^{11}C]PBB3

(A) In vitro autoradiograms of PS19 and non-Tg WT hindbrains (coronal sections) and AD frontal cortex. Fibrillar aggregates in the mouse brain stem and AD gray matter produced intense radiolabeling with both tracers, but nonspecific background signals were also observed at a considerably high level with the use of [^{11}C]PBB2. Binding of [^{11}C]PBB3 was profoundly abolished by the addition of nonradioactive PBB3 (10 μM).

(B) Autoradiographic labeling with intravenously injected [^{11}C]PBB2 and [^{11}C]PBB3 in PS19 (Tg) and WT mice. The brains were removed at 45 min after injection and were cut into sagittal slices. The autoradiographic section of PS19 brain was also stained with FSB. Arrows indicate the brain stem containing numerous tau inclusions displayed at intermediate and high magnifications.

(C) Sagittal and coronal PET images generated by averaging dynamic scan data at 60–90 min after intravenous administration of [^{11}C]PBB3. The images are overlaid on the MRI template (images of the template alone are presented at the bottom). Arrows and asterisks indicate the brain stem and striatum, respectively, and arrowhead denotes intense radiolabeling in the medial brain stem of the PS19 mouse.

(D) FSB staining of PS19 mouse brain shown in (C). Sagittal (left) and coronal (middle) images and a high-power view of fibrillar inclusions (right) are displayed. Corresponding to high-level retention of [^{11}C]PBB3 in PET scans, abundant FSB-positive lesions were found in the medial brain stem (arrow and arrowhead).

(E) Time-radioactivity curves (left) in the striatum (ST) and brain stem (BS) and BS-to-ST ratio of radioactivity (right) over the imaging time in PS19 (Tg; red symbols) and WT (black symbols) mice (n = 5 each). Vertical bars in the graphs denote SEs.

Scale bars, 1 cm (A and B, top, middle, and bottom left panels); 1 cm (C and D, left and middle panels); 100 μm (B, bottom middle panel); and 100 μm (B, bottom right panel and D, right panel). See also Figures S5, S6, and S7.

Detection of Tau Pathologies in Living Brains of AD Patients by Comparative PET Imaging with [^{11}C]PBB3 and [^{11}C]PIB

In order to compare the bindings of [^{11}C]PBB3 and [^{11}C]PIB to tau-rich regions in the human brain, in vitro autoradiography was carried out with sections of AD and control hippocampus. A notable difference in labeling between these two radioligands was observed in the CA1 sector and subiculum of the AD hippocampus, where fibrillar tau aggregates predominantly localized to NFTs and neuropil threads (Figure 7A).

We subsequently conducted an exploratory clinical PET study for patients with probable AD (n = 3) and age-matched cognitively normal control (NC) subjects (n = 3). All AD patients exhibited a marked increase in the retention of [^{11}C]PIB in

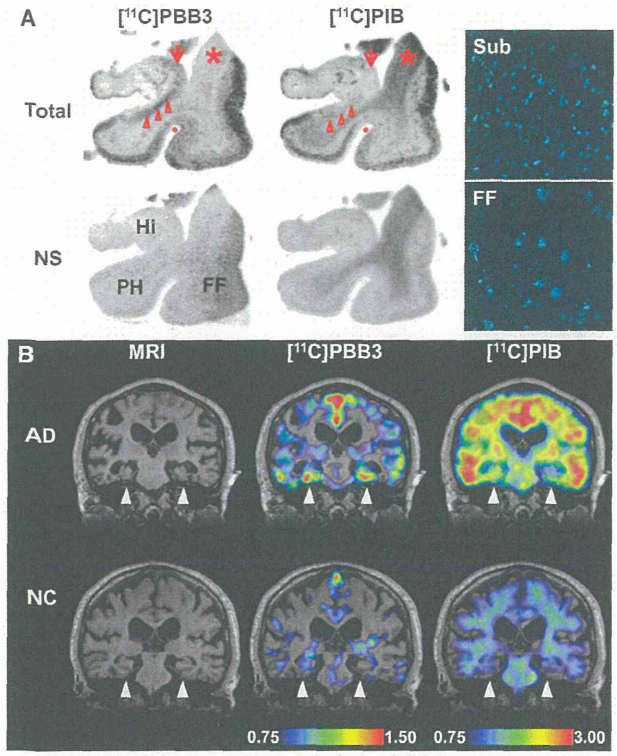

Figure 7. Accumulation of [^{11}C]PBB3 in the Hippocampal Formation of AD Patients Revealed by In Vitro Autoradiography and In Vivo PET

(A) Autoradiographic labeling of adjacent brain sections from an AD patient with 10 nM of [^{11}C]PBB3 (left) and [^{11}C]PIB (middle). The slices contain the hippocampus (Hi), parahippocampal gyrus (PH), fusiform gyrus (FF), and white matter (asterisks). Total binding (top) of [^{11}C]PBB3 and [^{11}C]PIB was markedly abolished (bottom) by addition of nonradioactive PBB5 (100 μM) and thioflavin-S (10 μM), respectively, except for the nonspecific (NS) labeling of white matter with [^{11}C]PIB. The hippocampal CA1 sector and subiculum displayed intense [^{11}C]PBB3 signals without noticeable binding of [^{11}C]PIB, and binding of [^{11}C]PBB3 in cortical areas flanking the collateral sulcus (identified by a red dot) and hippocampal CA2 sector (arrows) was also abundant relative to that of [^{11}C]PIB. FSB staining of amyloid fibrils in the sections used for autoradiography indicated the predominance of NFTs and diffuse plaques in the hippocampal subiculum (Sub) and fusiform gyrus (FF), respectively (right panels), supporting the strong reactivity of [^{11}C]PBB3 with AD NFTs.

(B) MRI (left) and PET imaging with [^{11}C]PBB3 (middle) and [^{11}C]PIB (right) performed in the same AD (top) and normal control (NC; bottom) subjects. Coronal images containing the hippocampal formation (arrowheads) are displayed. [^{11}C]PBB3- and [^{11}C]PIB-PET images were generated by estimating SUVRs at 30–70 min and 50–70 min after radiotracer injection, respectively, and were superimposed on individual MRI data. In the hippocampal formation, prominently increased retention of [^{11}C]PBB3 in the AD patient was in sharp contrast to the modest or negligible changes in [^{11}C]PIB binding as compared with NC. Scale ranges for SUVRs were 0.75–1.50 ([^{11}C]PBB3) and 0.75–3.00 ([^{11}C]PIB).

See also Figure S9.

plaque-rich areas, and all NC were negative for this PET assay. These subjects then received a [^{11}C]PBB3-PET scan, and the [^{11}C]PIB and [^{11}C]PBB3 images were compared in the same individuals. Intravenously injected [^{11}C]PBB3 was delivered to the brain tissue despite its relatively rapid metabolism in humans (Figures 9A and 9B). Unlike [^{11}C]PIB, [^{11}C]PBB3 showed minimal nonspecific binding to white matter and other anatomical structures with high myelin content, although it accumulated in dural venous sinuses in control and AD brains (Figures 7B, 8, and 9B). Time courses of regional radioactivity (Figures 9C and 9D; Figures S8A and S8B) and the standardized uptake value ratio (SUVR) to the cerebellum (Figures S8C and S8D) demonstrated accumulation of [^{11}C]PBB3 in several brain regions of AD patients as compared to controls (definition of these VOIs is indicated in Figure S8E). In agreement with autoradiographic findings, binding of [^{11}C]PBB3 to the medial temporal region, including the hippocampus, contrasted strikingly with the low-level retention of [^{11}C]PIB in this area (Figure 7B). There was a slight increase in the retention of [^{11}C]PBB3 primarily in the medial temporal region of a control subject with a loss of several points in Mini-Mental State Examination (MMSE) (subject 3 in Figure 8), appearing similar to the tau pathology at Braak stage III/IV or earlier (Braak and Braak, 1991), distinct from the lack of enhanced [^{11}C]PIB signals. Indeed, mild increase of medial temporal SUVR (Figure 9E) contrasted with unremarkable change in lateral temporal and frontal SUVRs in this subject (Figures 9G and 9H). Signals of [^{11}C]PBB3 were also intense mainly in the limbic region of a subject with early AD (subject 4 in Figure 8), but profound and moderate increases of SUVRs were also observed in the lateral temporal and frontal cortices, respectively, of this case (Figures 9G and 9H), resembling the localization of tau deposits at Braak stage V/VI (Braak and Braak, 1991). With the further cognitive decline as scored by MMSE (subjects 5 and 6 in Figure 8), additional increase in the retention of [^{11}C]PBB3 was found in the medial temporal region, precuneus, and frontal cortex (Figures 9E, 9F, and 9H). Meanwhile, a substantial decline of [^{11}C]PBB3 binding was noted in the lateral temporal cortex of subject 6 (Figures 8 and 9G). The SUVRs in the medial temporal region, precuneus, and frontal cortex were consequently well correlated with the decline of MMSE scores (Figures 9E, 9F, and 9H). In distinction with [^{11}C]PBB3-PET data, there was no overt association between the binding of [^{11}C]PIB and disease severity in AD patients (Figure 8), consistent with previous observations. These data support the potential utility of [^{11}C]PBB3 for clarifying correlations between the distribution of tau deposition and the symptomatic progression of AD.

As in vitro fluorescence staining indicated that PBB3 was reactive with not only tau lesions but also several types of senile plaques, particularly dense core plaques, density of binding sites, and affinity of [^{11}C]PBB3 for these sites were quantified by autoradiographic binding assays with hippocampal and neocortical sections of AD brains enriched with NFTs and senile plaques, respectively. These analyses demonstrated that specific radioligand binding sites were primarily constituted by high-affinity, low-capacity binding components in NFT-rich regions and low-affinity, high-capacity binding components in plaque-rich regions (Figures S9A and S9B). A subsequent simulation for radioligand binding in an area containing these two types of binding sites at a ratio of 1:1 indicated that the selectivity of [^{11}C]PBB3 for NFTs versus plaques may be inversely associated with concentration of free radioligands (Figure S9C). In a range of free concentration in the brain achievable

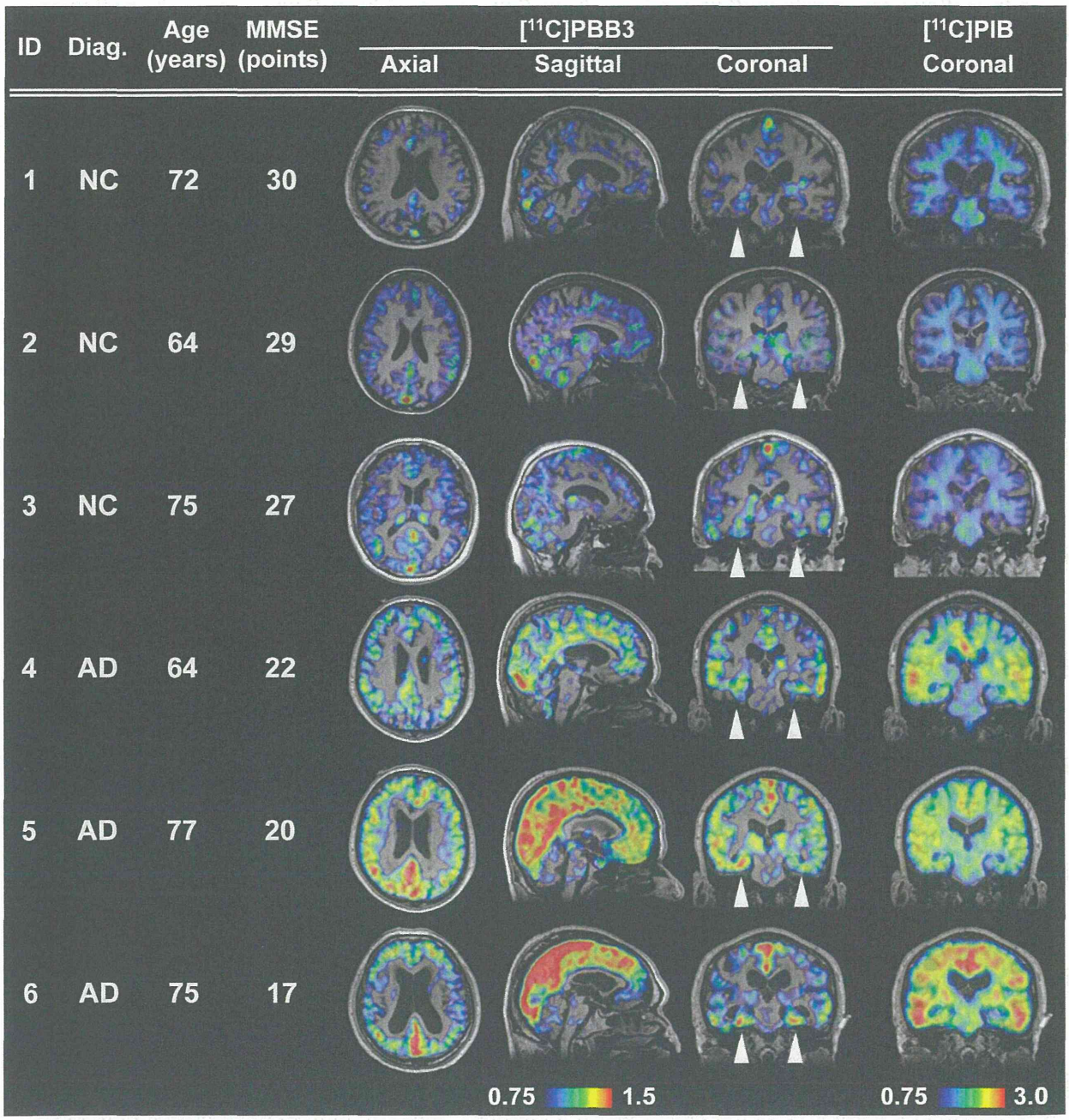

Figure 8. Orthogonal [^{11}C]PBB3-PET Images in All Human Subjects Examined in the Present Exploratory Clinical Study

Data are displayed as parametric maps for SUVR. The [^{11}C]PBB3 binding to the hippocampal formation (arrowheads) was increased consistently in AD patients in contrast to minimum radiotracer retention in normal control (NC) subjects with MMSE scores of 29–30 points (subjects 1 and 2). Another NC subject with an MMSE score of 27 points (subject 3) was negative for [^{11}C]PIB-PET but exhibited slight accumulation of radiotracer signals primarily around the hippocampus, resembling fibrillar tau deposition at Braak stage III/IV or earlier. Sagittal slices around the midline illustrate that radioligand signals were the most intense in the limbic system but began to expand to the neocortex in a patient with the mildest AD (subject 4), in agreement with the tau pathology at Braak stage V/VI, and was further intensified in most neocortical areas, corresponding to Braak stage VI, apparently as a function of the disease severity assessed by MMSE (subjects 5 and 6). The AD patient with the lowest MMSE score (subject 6) displayed a less profound increase of [^{11}C]PBB3 retention in the lateral temporal and parietal cortices than did the other two AD cases, and this is attributable to marked cortical atrophy in this individual and/or toxic loss of tau-bearing neurons in these brain areas at an advanced pathological stage. In contrast to the spatial profiles of [^{11}C]PBB3 binding, the distribution of [^{11}C]PIB signals appeared unchanged among AD subjects. See also Figure S9.

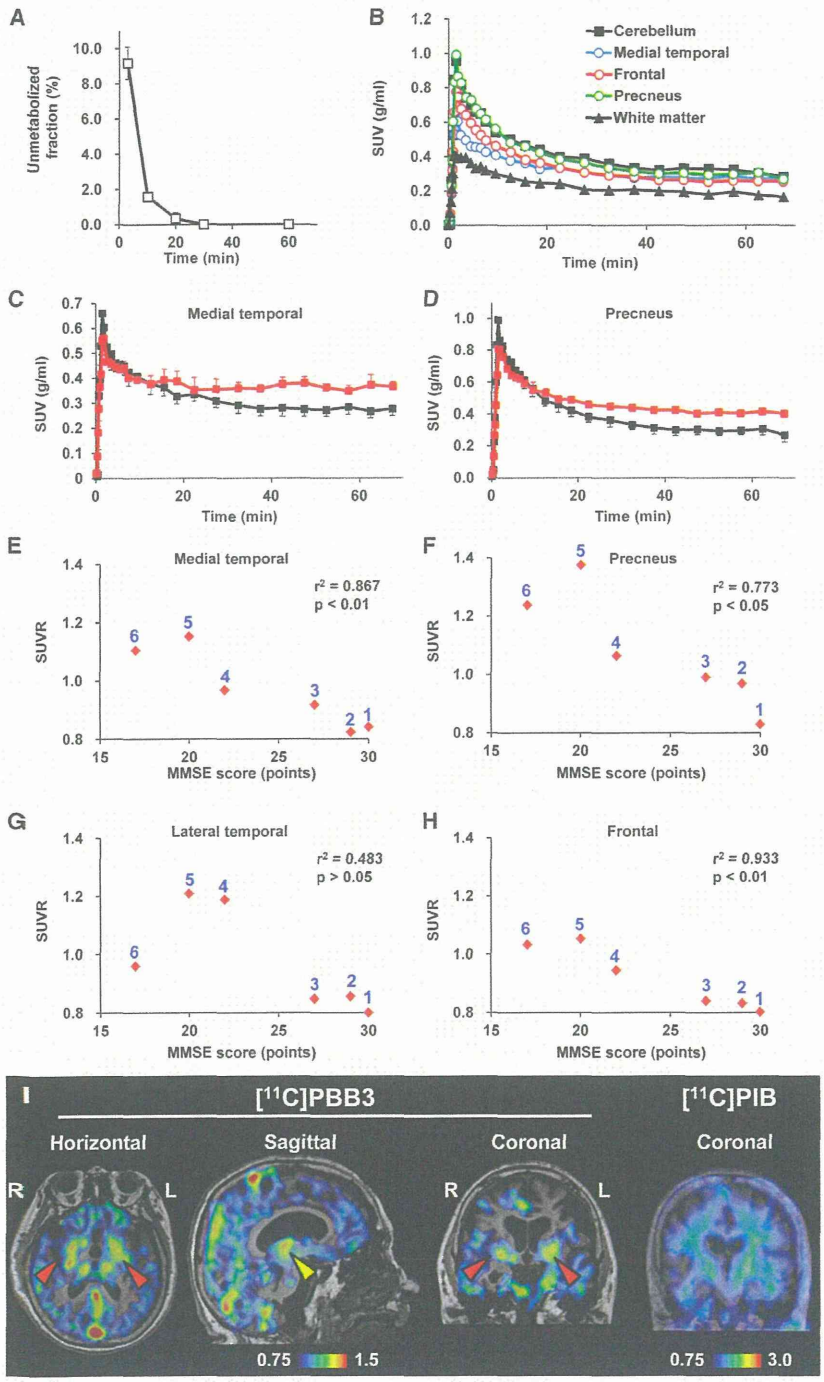

Figure 9. Pharmacokinetic Profiles of [^{11}C]PBB3 Administered to Humans and PET Images of a Patient Clinically Diagnosed as Having Corticobasal Syndrome

(A) Time course of unmetabolized [^{11}C]PBB3 fraction in plasma following intravenous radiotracer injection. The plot was generated by averaging data from six individuals.

(B) Time-radioactivity curves in different brain regions of cognitively normal control subjects over 70 min after intravenous injection of [^{11}C]PBB3. Data were generated by averaging values in two individuals and are presented as standard uptake values (SUVs).

(C and D) Comparisons of time-radioactivity curves in the medial temporal region (C) and precuneus (D) of normal controls (black symbols and lines; n = 3) and AD patients (red symbols and lines; n = 3).

(E–H) Scatterplots illustrating correlation of SUVRs with MMSE scores in the medial temporal region (E), precuneus (F), and lateral temporal (G) and frontal (H) cortices. Numbers beside symbols denote subject ID as indicated in Figure 8. Coefficients of determination (r^2) and p values by t test are displayed in graphs.

(I) [^{11}C]PBB3- and [^{11}C]PIB-PET images in a subject with clinical diagnosis of corticobasal syndrome. Images were generated as in Figures 7 and 8. Accumulation of [^{11}C]PBB3 was noticeable in the basal ganglia (red arrowheads) with right-side dominance and an area containing the thalamus and midbrain (yellow arrowhead).

Vertical bars in the graphs represent SEs. See also Figures S8 and S9.

at a pseudoequilibrium state in human PET imaging (<0.2 nM), [^{11}C]PBB3 is presumed to preferentially bind to tau lesions relative to *in vitro autoradiographic* (~1 nM) *and fluorescence* (>100 nM) labeling.

We also estimated contribution of [^{11}C]PBB3 bound to dense core plaques to total radiosignals in the neocortical gray matter of AD patients, by conducting autoradiography and FSB histochemistry for the same sections. Radiolabeling associated with dense cored plaques accounted for less than 1% and 3% of total gray matter signals in the temporal cortex and precuneus, respectively (Figures S9D–S9H). Moreover, fluorescence labeling of adjacent sections with PBB3 demonstrated that approximately 2% and 5% of total gray matter fluorescence signals were attributable to PBB3 bound to dense core plaques in the temporal cortex and precuneus, respectively. Hence, dense cored plaques were conceived to be rather minor sources of binding sites for [^{11}C]PBB3.

Finally, PET scans with [^{11}C]PBB3 and [^{11}C]PIB were conducted for a subject clinically diagnosed as having corticobasal syndrome. Retention of [^{11}C]PIB stayed at a control level, but notable accumulation of [^{11}C]PBB3 was observed in the neocortex and subcortical structures (Figure 9I), providing evidence for in vivo detection of tau lesions in plaque-negative